LIMNOLOGY
and
OCEANOGRAPHY: METHODS

Limnol. Oceanogr.: Methods 5, 2007, 309–316

A novel radioactivity microsensor for high spatial resolution measurements of β radiation

Heinz Filthuth[1], Gabriele Eickert[1], Paul Faerber[1], Henk M. Jonkers[1,2], Lubos Polerecky[1], and Dirk de Beer[1]*
[1]Max-Planck Institute for Marine Microbiology, Celsiustrasse 1, D-28359 Bremen, Germany
[2]Delft University of Technology, P.O. Box 5048, 2600 GA Delft, The Netherlands

Abstract

We developed a microsensor for the detection of β-radiation with submillimeter spatial resolution. The microsensor consists of a scintillating sphere (diameter 100–300 μm) glued to a tip of an optical fiber (core diameter 140 μm) enclosed in a thin glass capillary. The scintillating sphere was made by embedding YLu scintillation powder and TiO_2 light scattering particles in a methacrylate matrix. Photons generated in the scintillator by the β-particles are guided through the fiber and detected by a photomultiplier connected to the opposite fiber end. The photon counts generated by the photomultiplier are linearly proportional to the volume-specific radioactivity in the sample. The background signal can be suppressed practically to zero if two fibers connected to two photomultipliers working in coincidence are used. This, however, results in slightly diminished sensor performance (lower sensitivity and signal-to-noise ratio). As examples of applications, the diffusion coefficients of $^{36}Cl^-$, $H^{14}CO_3^-$, and $^{45}Ca^{2+}$ in agar-solidified saline water were measured, and the depth distribution of primary productivity in an intact microbial mat was determined from vertical profiles of ^{14}C after incubation in the light using $H^{14}CO_3^-$ as tracer.

Microsensors allow minimal invasive measurements of concentrations of chemical species with submillimeter spatial resolution. For more than three decades, microsensors have been an indispensable tool employed for the quantification of microbial processes in a variety of biological systems, such as sediments, biofilms, microbial mats, and coral tissues. In these systems, mass transfer resistance and high conversion rates lead to steep gradients of substrates and products, and to highly localized conversions. For example, oxygen penetrates in active biofilms less than 100 μm, in sediments mm to cm, while in microbial mats photosynthesis can be limited to the top 1 mm. Therefore high resolution analyses are needed to assess the stratification of the involved reactants and determine activity distributions. Since microsensors are very small, having tip sizes of 1–20 μm, they do not significantly change the chemical distribution nor disturb the sample. First, microsensors employed electrochemical principles to transduce the chemical species concentration to a measurable electrical signal (Bungay et al. 1969). A combined microelectrode for O_2, reliable for environmental studies, was developed and applied in microbial ecology by Revsbech (Revsbech 1983; Revsbech 1989). Subsequently, a large suite of microsensors, based on electrochemical and optical transduction, has been developed for various chemical compounds and physical parameters such as light, temperature, and diffusion coefficient (Kühl and Revsbech 1999). The development of microsensors for more physico-chemical species remains an active and dynamic research field (Gieseke and De Beer 2004). At present, approximately 20 different parameters can be measured.

Here we report on the development of a radioactivity microsensor that allows the detection of β-radiation, and thus the detection of all compounds that are labeled with radio-isotopes decaying through the emission of a β-particle, in an intact sample with submillimeter spatial resolution. The sensor opens the possibility to study the transport, uptake, and binding of a wide range of metabolites in diverse biological

*To whom correspondence should be addressed. Lubos Polerecky, Max-Planck Institute for Marine Microbiology, Celsiustrasse 1, D-28359 Bremen, Germany. lpolerec@mpi-bremen.de, Tel: 0049-421-2028 834, Fax: 0049-421-2028 690

Acknowledgments

We thank Bo Barker Jørgensen for the initial impulse for the development of this sensor and for his continuous support of this project; Fritz Berthold and Wilfried Reuter from Berthold Technologies for valuable discussions and for supplying the coincidence unit; Friedrich Widdel, Timothy Ferdelman, Armin Gieseke, Stefan Jansen, and Volker Meyer for valuable support; Werner Zinsser from Zinsser Analytic for useful advise and for providing the scintillating material. This work would not have been realized without the technical support of W. D. Schlatter, Lucia Linssen, Alfredo Placci, and Catherine Moine from CERN, which we greatly appreciate. We also thank two anonymous reviewers for their valuable comments on the manuscript. The financial support was provided by the Max-Planck Society.

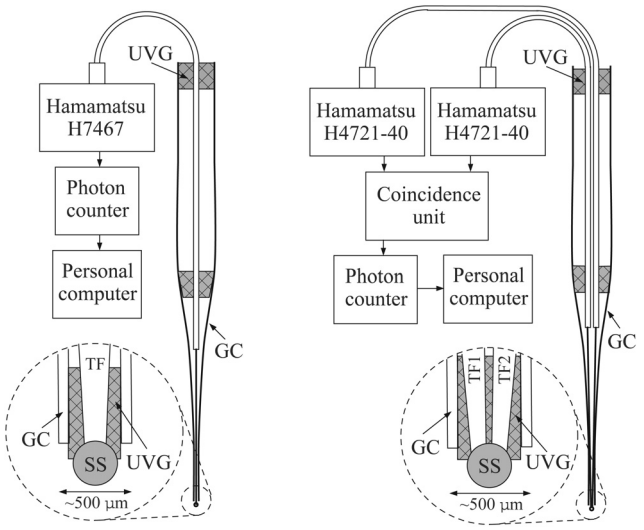

Fig. 1. Schematic diagrams of the single-fiber (A) and double-fiber (B) radioactivity microsensors. SS—scintillating sphere; TF—tapered fiber; UVG—UV-curable glue; GC— glass capillary with a prolonged shaft.

systems ranging from sediments, biofilms, and microbial mats to animal or plant tissues.

Materials and Procedures

Sensor construction—The microsensor for β-radiation was constructed in a similar way as the scalar irradiance microprobe (Lassen et al. 1992). A glass optical fiber (core diameter 140 μm, length 1–1.5 m; Radial) with attached ST connectors was cut in half and the plastic shield and cladding were removed approximately 5 cm from the cut-off ends of the fiber. The fiber ends were subsequently tapered to a diameter of ~30 μm using a fusion splicer (Siemens AG). A scintillating cocktail was prepared by mixing 600 mg of Lu-Y powder (Zinsser Analytic; 3 μm grains) with 80 mg of the cocktail used for the preparation of the scalar irradiance microprobe, which contains TiO_2 particles and methacrylate dissolved in xylene (Lassen et al. 1992). Single-fiber and double-fiber sensors were designed and used (Fig. 1).

The single-fiber sensor was prepared by depositing a scintillating sphere (diameter 100–200 μm) onto the tapered fiber tip (Fig. 1A). The deposition was done by dipping the fiber tip several times into the scintillating cocktail. After the solvent evaporated and the sphere hardened, the fiber end together with the sphere was optionally painted black to minimize the influence of the light generated outside the sphere (e.g., Cherenkov radiation; see Assessment). For mechanical protection and convenient handling, the fiber was inserted and glued by UV-curable glue (Loctite) inside a glass capillary with a prolonged shaft, with the sphere protruding ~100 μm out of the shaft. The external diameter of the glass capillary was 200–300 μm. The sensor was connected to a sensitive photomultiplier (PM) (H7467, Hamamatsu, quantum efficiency(QE) 20%). The photon counts generated in the PM were processed by an electronic unit.

The double-fiber sensor, constructed in order to reduce the background signal due to non-specific photon generation, was made by first gluing together two tapered fiber ends with UV-curable glue (Loctite) and then depositing the scintillating sphere (diameter ~300 μm) onto the double-fiber tip (Fig. 1B). The sensor was inserted in a ~500 μm glass capillary as described above. Each fiber was connected to a PM (H4721-40, Hamamatsu, QE 40%). Photon counts generated in the two independent PMs were processed by an electronic unit which implemented a coincidence circuit that registered a valid β-particle detection event only when the photon arrival events generated by both photomultipliers were within ~100 ns from each other.

A standalone Microsoft Windows-based program was developed to transfer the photon counts from the electronic unit to a personal computer through the RS 232 (serial) interface (Polerecky, unpubl. data). In addition to the accumulation and averaging of the photon counts over user-specified time periods, the software allowed automatic control of a motorized linear positioner (VT-80, Micos), to which the sensors were mounted during experiments.

Sensor calibration and characterization—The response of the radioactivity microsensor toward volume-specific radioactivity, R_v, was studied in detail for ^{36}Cl. Calibration solutions with R_v in the range of 50–800 kBq cm^{-3} were prepared by diluting the standard $^{36}Cl^-$ solution (4.17 MBq cm^{-3} $^{36}Cl^-$ in 0.2 M HCl; Amersham) in Milli-Q water. The sensor was inserted into each calibration cocktail for 1 h and the photon counts were accumulated over 10 min intervals. For the other studied radio-labeled specimens, ^{14}C and ^{45}Ca, the shape of the calibration curve was assumed to be the same as for ^{36}Cl, except for a factor characteristic for each particular specimen. This factor was determined by measuring the photon counts by the sensor inserted directly into the respective standard solutions: 37 MBq cm^{-3} (1.8 GBq $mmol^{-1}$) $NaH^{14}CO_3$ at pH 9.5 (Perkin Elmer Life and Analytical Sciences) for $H^{14}CO_3^-$, and 77.1 MBq cm^{-3} (0.185–1.85 GBq mg^{-1}) $^{45}CaCl_2$ (Amersham) in aqueous solution for $^{45}Ca^{2+}$. All measurements were conducted in a light-tight black box to exclude photons of the ambient light. The sensor was rinsed with water before it was inserted into the next calibration cocktail. The volume-specific radioactivities (R_v), of the calibration solutions were measured using a Packard 2500 TR liquid scintillation counter.

The sensor performance was characterized using the following Figures of merits: (i) sensitivity, *S*, defined as the ratio between the change in signal (in counts per minute, cpm) and the corresponding change in R_v (in kBq cm^{-3}); (ii) signal-to-noise ratio, *SNR*, defined as the ratio between the signal and its standard deviation measured at a particular R_v; (iii) limit of detection, *LOD*, defined as $3\sigma_0/S$, where σ_0 is the standard deviation of the signal measured at zero radioactivity; and (iv) background, *BKG*, i.e., signal measured at zero R_v.

Diffusion experiments—The sensor was used to measure the diffusion coefficients of selected ions (Cl^-, HCO_3^-, and Ca^{2+}) in agar-solidified water. Radioactive agar solutions were prepared by mixing standard radioactive solutions of known radioactivity with 0.5 wt% agar in 10 mM $NaHCO_3/Na_2CO_3$-buffered saline water (1 M NaCl, pH 8). The buffer strength and salinity of the water used here were similar to those in the natural saline water used in the primary productivity experiments with a microbial mat (see below). Solutions of $^{36}Cl^-$ (500 kBq cm^{-3}), $H^{14}CO_3^-$ (5 MBq cm^{-3}), and $^{45}Ca^{2+}$ (5 MBq cm^{-3}), prepared from the standard solutions listed above, were used. A cut-off syringe core (inner cross-section 1 cm^2) was fixed in a vertical position by a clamp and filled with 2 mL of non-radioactive agar (0.5 wt%). The radioactivity sensor was attached to a manual micromanipulator fixed to a heavy stand and the sensor tip was positioned 1 cm into the agar layer. Subsequently, 1 mL of the still warm (40° C) and liquid radioactive agar was gently poured on top. Due to the small volume, temperature of this agar layer equilibrated with the rest of the sample within a few minutes. The setup was enclosed in the black box and the photon counting was started within 1 min after the radioactive agar addition. Photon counts were accumulated over 10 min intervals and recorded as counts per min (cpm) until a constant signal was reached (up to ~5 days). The temperature was kept at 20 ± 0.5° C (room temperature) during the measurement. Drying out of the agar was prevented by enclosing a glass of water inside the box to keep the air humidity saturated. Experiments were conducted with both single-fiber and double-fiber radioactivity sensors.

The transport of the radioactive ions in the agar was modeled by the one-dimensional time-dependent diffusion equation. Diffusion was the only transport process, as advection and convection were negligible in the agar matrix, and were further minimized by avoiding temperature variations and mechanical vibrations. Assuming that the entire agar volume was homogeneous with respect to its diffusion coefficient, the time-dependent diffusion equation could be solved analytically using the variable separation method. We considered $c(z,0) = c_{init}$ in the top agar layer ($-z_a \le z \le 0$) and $c(z,0) = 0$ in the bottom agar layer ($0 < z \le 2z_a$) as the initial conditions, and $\partial c/\partial z = 0$ for $z = -z_a$ and $z = 2z_a$ (i.e., zero fluxes at both region boundaries; z_a = 1 cm) at all times $t \ge 0$ as the boundary conditions. Here, $c(z,t)$ denotes the analyte concentration in location z at time t, z_a is the thickness of the top agar layer. By expressing the solution as Fourier series and matching the above initial and boundary conditions, the concentration at the sensor tip position (at z_0 = 1 cm) takes the form

$$c(z_0,t) = \frac{c_{init}}{3} + \sum_{m=1}^{\infty} \frac{2c_{init}}{m\pi} \sin a_m \cos(a_m z_0 / z_a) \exp(-Dta_m^2 / z_a^2),\ a_m = m\pi / 3. \quad (1)$$

The best estimate of the diffusion coefficient (D) of the respective radio-labeled specimen in agar was obtained by fitting the measured sensor signal with function (1), which was done in Matlab (MathWorks).

^{14}C-incorporation experiment—The sensor was also used to map (in a dense microbial mat with high spatial resolution) the carbon accumulation which occurred as metabolic carbon fixation and/or carbonate precipitation, both a consequence of mat's photosynthetic activity (Ludwig et al. 2005). Microbial mat samples were collected from the hypersaline lake La Salada de Chiprana (Spain) in September 2005. Prior to the experiments, the samples were stored in an aquarium filled with aerated water from Lake Chiprana (salinity 80 g L^{-1}, temperature 20° C) and illuminated with photosynthetically active radiation (PAR; 400–700 nm, downwelling irradiance 250–350 μmol photons m^{-2} s^{-1}, 16 h light/8 h dark regime). More detailed description of the mat is given elsewhere (Jonkers et al. 2003). In short, the mat consisted of layers with distinct coloration and microbial composition. The top 0–2 mm layer was light-green and dominated by *Chloroflexus*-like filamentous bacteria, diatoms (*Nitzschia* and *Navicula* spp.), and three types of cyanobacteria, unicellular Halothece-like cells (1–2 μm diameter), filamentous *Oscillatoria*–like cells (2 μm diameter), and filamentous *Pseudoanabaena*-like cells (1.5 μm diameter). The 2–6 mm layer appeared dark-green and was dominated by filamentous *Oscillatoria*-like cyanobacteria of various diameters (1, 2, and 5 μm). The 6–8 mm depth layer appeared purple and contained high biomass of anoxygenic phototrophic purple sulfur bacteria. Below 8 mm, the mat was black due to abundant iron sulfide precipitates.

Mat samples (~2 cm thick) were collected by syringe cores (inner cross-section 1 cm^2) and covered with water from Lake Chiprana to which 4.2 MBq $H^{14}CO_3^-$ was added. One sample was illuminated by PAR (downwelling irradiance 300 μmol photons m^{-2} s^{-1}, 16 h light/8 h dark regime), while the other was stored in the dark. After 4 d of incubation, vertical profiles of ^{14}C were measured in the mats using both the single-fiber and double-fiber sensors. Automatic movement of the sensor was done using a motorized linear positioner (VT–80, Micos) controlled by a computer. During the measurement, the setup was enclosed in a light-tight black box and temperature was kept constant at 20 ± 0.5° C (room temperature). Photon counts were accumulated over 10 min intervals at each depth. A total profile over a depth of 12 mm (in 250 μm steps) was accomplished in 8 h.

Assessment

Sensor construction—The best performance of the radioactivity microsensor was achieved by using LuY in powder form (3 μm grains) as scintillator, which was embedded in a methacrylate matrix. Additionally, TiO_2 particles were embedded in the matrix to improve, through enhanced scattering, coupling of photons into the optical fiber and thus increase the signal. Before this design, an organic scintillator (BF12) or Lu or Y crystals (1–2 mm^2) glued directly to the fiber tip also were tested. However, this configuration did not lead to satisfactory

Table 1. Endpoint energy, E_e, most probable energy, estimated as $E_m \approx E_e/2$, and the corresponding typical penetration range in water, (R_w) of beta-particles emitted by selected "pure" beta-minus sources. Energy data taken from Lederer and Shirley (1978), penetration range calculated from E_m using the formula in *US Public Health Service (1970). Radiological Health Handbook. Publ. No. 2016. Bureau of Radiological Health, Rockville, MD.*

Nuclide	E_e (MeV)	E_m (MeV)	(R_w) (μm)
^{14}C	0.156	0.078	≈ 80
^{33}P	0.248	0.124	≈ 250
^{35}S	0.167	0.084	≈ 80
^{36}Cl	0.714	0.307	≈ 800
^{45}Ca	0.252	0.126	≈ 250

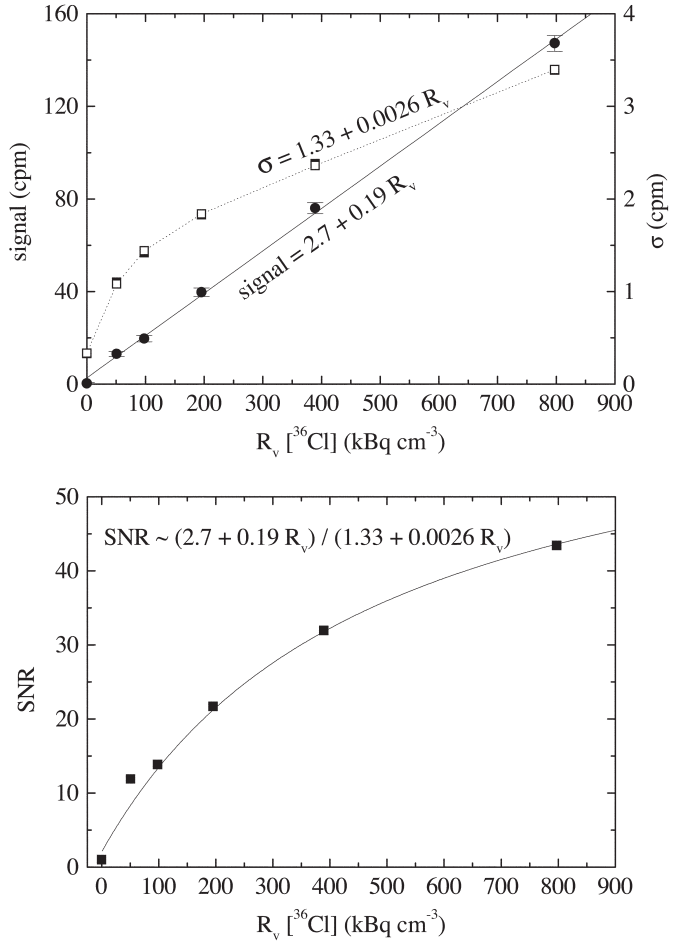

Fig. 2. Example of a calibration plot for a double-fiber radioactivity microsensor. (A) Sensor signal (solid circles) and its standard deviation, σ (open squares and error-bars), are plotted against the volume-specific radio activities of the ^{36}Cl calibration solutions, R_v[^{36}Cl]. Sensor sensitivity was ≈ 0.19 cpm kBq^{-1} cm^3, as derived from the slope of the linear fit (solid line). Standard deviation of the signal, calculated from six measurements taken at each R_v, varied approximately linearly with R_v at $R_v \geq 200$ kBq cm^{-3} (see formula next to the dashed line). (B) Signal-to-noise ratio as a function of R_v derived from the data in panel (A). The formula for the best fitting hyperbola (solid line) is shown in legend.

results (the photon counts obtained were extremely low) and was thus not pursued further.

During the initial stage of the sensor development, most notably during the diffusion experiments in agar, photons were detected by the photomultiplier connected to the fiber even if no scintillator was attached to the fiber tip and the sensor was in complete darkness. This 'ghost' signal was attributed to Cherenkov radiation generated in the cuvette and/or inside the sensor fiber by traversing high-energy β-particles. This undesirable background signal was suppressed when a thin layer of black paint was deposited on both the scintillating sphere and the fiber around the sensor tip. This treatment, however, also resulted in considerably diminished sensor sensitivity, especially when detecting low-energy β-particles generated by ^{45}Ca or ^{14}C. Thus, painting of the sensor was employed and is recommended only for the detection of radio-isotopes that emit highly energetic β-particles (e.g., ^{36}Cl, Table 1).

Sensor calibration and characterization—In general, sensor signal (cpm) increased linearly with the volume-specific radioactivity of the $^{36}Cl^-$ calibration solutions (Fig. 2A, solid symbols). The increase of the signal standard deviation, σ, with R_v was non-linear at lower R_v and became linear at higher R_v (Fig. 2A, open symbols). Consequently, the increase of *SNR* with R_v followed a hyperbolic function, which asymptotically approached a specific value of SNR_{max} at high R_v (for the particular sensor shown, $SNR_{max} = 0.19/0.0026 \approx 73$; Fig. 2B).

In general, sensitivity, *SNR*, and *LOD* of the sensor depended strongly on the radioactive specimen (Table 2). For the particular sensor whose calibration toward $^{36}Cl^-$ is shown in Fig. 2, sensitivity toward ^{36}Cl was ~0.19 cpm kBq^{-1} cm^3, while it was ~35 and ~110 times lower toward ^{45}Ca and ^{14}C, respectively. Consequently, the lowest *LOD* was achieved for ^{36}Cl (~5.2 kBq cm^{-3}), while *LOD* for ^{45}Ca and ^{14}C was ~35 and ~110 times higher, respectively. The highest *SNR* was achieved for ^{36}Cl (~43 at 0.8 MBq cm^{-3}), while it was much lower for ^{45}Ca (~20 at 6.7 MBq cm^{-3}) and ^{14}C (5.6 at 3.0 MBq cm^{-3}).

Sensor performance with respect to sensitivity, *SNR*, *LOD*, and *BKG* varied considerably among different sensors (Table 2), although no visual differences in the geometry (size, shape) of the spherical tip were observed, as checked using a dissection microscope. Single-fiber sensors had a relatively large background signal (30–125 cpm), while the background was negligible (~0.3 cpm) for the double-fiber sensors. Double-fiber sensors had a few times lower sensitivity than single-fiber sensors, whereas the absolute values of *LOD* and *SNR* were similar for both sensor designs. The sequence of sensitivity and *LOD* toward ^{36}Cl, ^{45}Ca and ^{14}C was the same for both sensor types; the lowest *LOD* was achieved for ^{36}Cl, whereas *LOD* for ^{45}Ca and ^{14}C was at least an order of magnitude higher. Similarly, volume-specific radioactivities of ^{45}Ca and ^{14}C had to be ~10 times higher than for ^{36}Cl to achieve comparable *SNR* for both sensor types.

It is worth noting that the sensor sensitivity is highest for the radio-isotope with the longest penetration range (compare

Table 2. Figures of merits characterizing the performance of radioactivity microsensors. Data were compiled from the measurements conducted with *N* different sensors. *S*—sensitivity; *SNR*—signal-to-noise ratio at volume-specific radioactivity; *LOD*—limit of detection; *BKG*—background signal, i.e., signal at zero radioactivity.

	S (cpm kBq^{-1} cm^3)	SNR (at MBq cm^{-3})	LOD (kBq cm^{-3})	BKG (cpm)	N	sensor type
^{36}Cl	0.19	43 (0.8)	5.2			
^{45}Ca	0.0055	20 (6.7)	180	≈ 0.3	1†	2-fiber
^{14}C	0.0017	5.6 (3.0)	580			
^{36}Cl	0.32–0.58	13–72 (0.14)	5.7–20	55–125	7	1-fiber
^{36}Cl	0.16–0.19	17–30 (0.14)	5.2–14	≈ 0.3	2	2-fiber
^{45}Ca	0.018–0.047	19–43 (1.4)	96–270	30–65	2	1-fiber
^{45}Ca	0.0055–0.029	12–20 (1.4)	180–210	≈ 0.3	2	2-fiber
^{14}C	0.012–0.088	11–34 (1.0)	91–270	60–90	2	1-fiber
^{14}C	0.0017–0.016	5.6–37 (1.4)	110–580	≈ 0.3	2	2-fiber

†Data correspond to the same 2-fiber sensor.

Tables 1 and 2). This is understandable on the basis that the longer penetration range implies greater volume around the sensor tip from which β-particles travel toward the scintillating sphere where they are detected. Furthermore, greater energy of β-particles results in more photons per β-particle generated in the scintillating material, which also contributes to greater sensitivity. On the other hand, the longer penetration range also implies lower spatial resolution.

Diffusion experiments—The signal measured by the radioactivity microsensor during the agar-on-agar diffusion experiments agreed very well with the theoretical model (Fig. 3). This indicates that the model's assumptions, leading to Eq. (1), were fulfilled and the sensor performance as well as the experimental conditions stayed constant during the whole duration of the experiment (~4 days). The absolute level and the dynamic range of the signal varied when different sensors were used, which was caused by the variable background signals and sensor sensitivities (see above). However, the shape of the signal's temporal evolution measured for the same radiolabeled specimen was reproducible (Fig. 3A). Consequently, the diffusion coefficients determined from the best fits of the experimental data obtained by different sensors agreed with better than 5% precision (see legend in Fig. 3A).

The highest diffusion coefficient in agar was found for $^{36}Cl^-$, while the coefficients for $H^{14}CO_3^-$ and $^{45}Ca^{2+}$ were lower (Fig. 3B, Table 3). The absolute values of the diffusion coefficients found were somewhat lower than those reported in literature (Li and Gregory 1974). This can possibly be explained by the relatively high ionic potential of the 1M NaCl solution used in the diffusion experiments, since a high ionic potential is known to slow down ionic diffusion by increasing the thickness of the hydration layer of water molecules around the ion. The ratios between the diffusion coefficients of the different ions (Table 3), which are generally independent of the ionic potential, were similar to those reported in literature.

The diffusion measurements and their theoretical analysis were conducted in a medium with a constant diffusion coeffi-

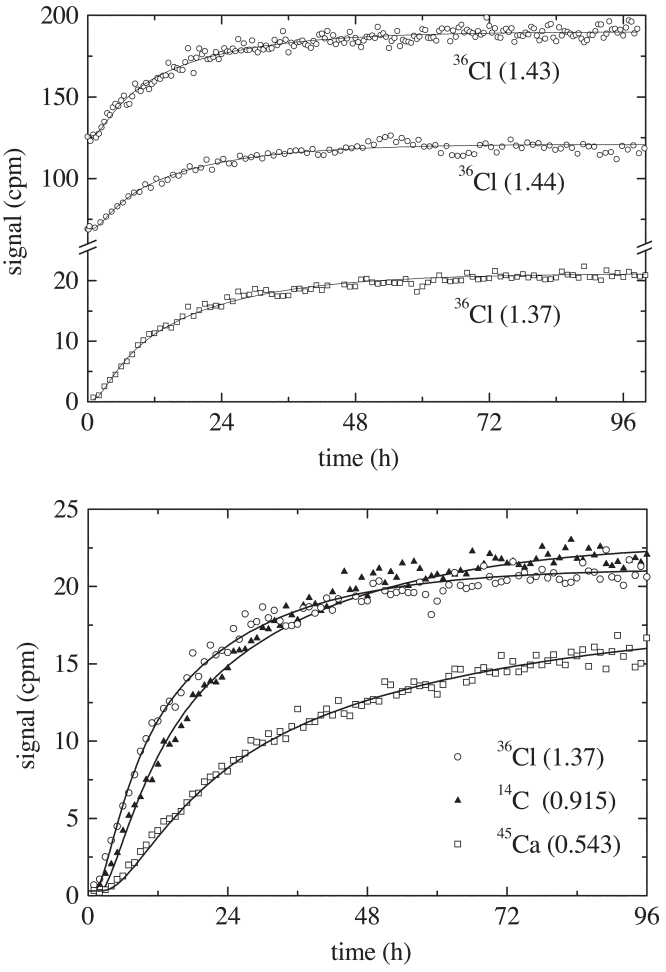

Fig. 3. Sensor signal as a function of time obtained by several radioactivity microsensors during diffusion experiments in agar. Each point corresponds to the photon-count signal accumulated over 10 min. (A) Examples of data obtained for ^{36}Cl by two different single- fiber sensors (circles) and a double-fiber sensor (squares). (B) Examples of data obtained for ^{36}Cl, ^{14}Cl, and ^{45}Ca by three different double-fiber sensors. The diffusion coefficients in 10^{-9} m^2 s^{-1}, derived from the best fits of the data by Eq. 1(lines),are shown in parentheses after the corresponding radio-labeled specimen.

Table 3. Comparison between the diffusion coefficients (in 10–9m2s–1) of ions in water measured in this work (at T = 20° C) and those reported by Li and Gregory (1974) (at T = 25° C).

ion	this work	Li and Gregory (1974)
Cl^-	≈ 1.40	2.03
$H^{14}CO_3^-$	0.915	1.18
Ca^{2+}	0.543	0.79
Cl^-:$H^{14}CO_3^-$:Ca^{2+}	2.6:1.7:1	2.6:1.5:1

cient throughout the entire volume. If the experiments were carried out in a medium with a variable diffusion coefficient, e.g., in sediment or a microbial mat covered with agar-solidified water (not presented here), the analytical solution (1) would not hold. In such case, the measured signal would have to be fitted with a numerical solution to the time-dependent diffusion equation (using the same initial and boundary conditions as above) parameterized by the unknown diffusion coefficient of the studied medium. The diffusion coefficient in the overlying agar should be determined beforehand by conducting the same agar-on-agar experiment as described here.

^{14}C-incorporation experiment—The vertical profiles of ^{14}C measured by the single-fiber radioactivity sensor in the microbial mat incubated in the light exhibited two distinct peaks at depths of ~1 mm and ~4 mm (Fig. 4A, squares). These peaks coincided with two distinct layers in the mat, the light-green surface layer (0–2 mm), dominated by diatoms, cyanobacteria, and *Chloroflexus*-like bacteria, and the lower dark-green layer (2–6 mm), dominated by cyanobacteria. No such peaks were observed in the dark-incubated mat (Fig. 4A, circles), indicating highly elevated and localized carbon assimilation rates in the light in comparison to the dark. This can be interpreted by considering that, in the light, phototrophic organisms such as diatoms, cyanobacteria, and purple sulfur bacteria, convert carbon dioxide and bicarbonate ions into organic material. Part of this material is incorporated in biomass, i.e., structural cell material, and part may be excreted in the form of extracellular but still structural polysaccharides or as truly dissolved organic matter. The rate of inorganic carbon fixation and subsequent compartmentalization is mainly determined by the quantity and (spectral) quality of the supplied light as well as the nutritional condition of the mat (Ludwig et al. 2006). Incubation of an illuminated mat with $H^{14}CO_3^-$ radiotracer should therefore result in immobilization of the tracer in mat zones where inorganic carbon is incorporated in structural organic matter by active photosynthetic and other autotrophic microorganisms. In such zones, radioactivity should accumulate, as fixed and converted tracer is replenished by diffusion from surrounding areas, which was demonstrated in our measurements.

A rather unexpected result was that no radiotracer incorporation was observed in the deeper mat regions (6–8 mm; Fig. 4A), which is inhabited by anoxygenic phototrophic purple sulfur bacteria. This specific group of bacteria is known to be

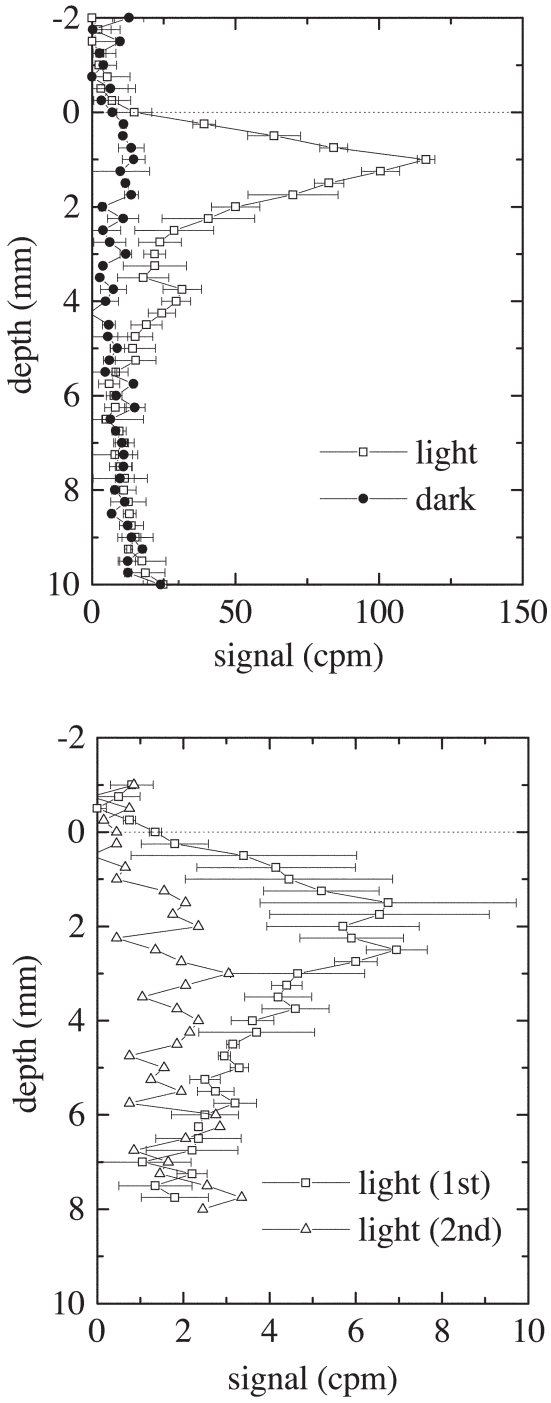

Fig. 4. Sensor signal as a function of depth measured by a single-fiber (A) and double-fiber (B) radioactivity microsensor in a microbial mat incubated for 4 d in the light (open symbols) and in the dark (filled symbols). The mat was covered with in situ water mixed with ≈5Mbq $H^{14}CO_3^-$ during incubation. Data in panel (A) represent mean values and standard deviations of four profiles measured in the same spot immediately after each other. Circles with error bars in panel (B) represent mean values and standard deviations of two profiles measured in different spots of the mat. Triangles in panel (B) show an example of a second profile measured in the same spot of the mat immediately after the measurement of the first profile. Background signal was subtracted from the data in panel (A).

able to fix inorganic carbon using the near infrared (NIR) part of the light spectrum, which penetrates much deeper into the mat than the visible light, and to be adapted to very low light intensities. A possible explanation for the negligible tracer accumulation observed can be that insufficient light intensities in the NIR region were applied during this experiment. Alternatively, high carbon turnover rates, which are typically found in deeper mat regions (Jørgensen and Cohen 1977), also could result in close to zero net incorporation rates.

The subsequent profiles measured by the single-fiber sensor in the same spot were reproducible, which is demonstrated by the low standard deviation of the data-points in Figure 4A. This was not the case for the double-fiber sensor, where the second profile measured immediately after the first one was significantly flatter (Fig. 4B, triangles) and where only one broader peak from 1 to 3 mm instead of two distinct peaks could be identified (Fig. 4B, squares). These effects, which were systematically observed in several locations across the mat, were caused by a hole that remained in the mat after the first profile was measured by the double-fiber sensor. This could have been caused either by a slightly larger diameter of the double-fiber sensor or, possibly, due to a loss of mat's 'flexibility' during the time between the measurements done with the single-fiber and double-fiber sensors (~2 months).

Although the carbon incorporation rates were determined only qualitatively in this work, quantitative assessment is also possible, e.g., by observing the tracer build-up while measuring a series of tracer concentration profiles during the incubation period. However, care should be taken when interpreting such data, especially because of the following two reasons. Firstly, ^{14}C may accumulate in the photosynthetic layer due to carbonate precipitation, which is known to be associated with photosynthetic activity in dense microbial systems like mats (Ludwig et al. 2005), leading to a possible overestimation of carbon fixation rates. Secondly, the rather long duration (a few hours) of the profile measurement in which the mat needs to be incubated in the dark is also critical for estimating primary productivity. During this prolonged dark incubation it cannot be excluded that heterotrophic metabolism leads to a remineralization of the ^{14}C fixed into organic carbon during the light incubation, potentially underestimating primary productivity. This experimental effect can, however, be minimized by measuring the build-up of the radioactivity signal over a smaller range of depths using greater steps, thus limiting the dark incubation period to several tens of min instead of several hours.

Discussion

Traditionally, β-imaging and scintillation counting have been used for qualitative and quantitative measurements of transport, binding, and accumulation of radio-labeled substrates in biological samples. These methods are destructive in nature. The novel radioactivity microsensor presented here offers a clear advantage, as it allows such measurements to be done on intact samples.

Two sensor designs were realized, a single-fiber and a double-fiber sensor, both having certain advantages and disadvantages. The single-fiber sensor allowed a smaller detector size (100–200 μm) than the double-fiber sensor (~300 μm) and exhibited generally greater sensitivity and a slightly better *SNR*. On the other hand, the background signal, which was relatively high and variable for a single-fiber sensor, was reduced practically to zero for the double-fiber sensor. *LOD*s were comparable for both sensor types (Table 2). Thus, the use of a single-fiber sensor is recommended if the sensor size and the general performance matter more during the measurement. In such case, the background signal, which is sensor specific but a priori unknown, will have to be determined before and after the experiment. On the other hand, if the (zero) level and stability of the background signal are essential, than the double-fiber sensor should be used.

The spatial resolution of the microsensor is determined not only by the size of the sensor tip (diameter of 100–300 μm in this work) but also by the typical penetration range of the β-particle in the studied sample. The actual resolution achieved in the measurement is equal to whichever of the two quantities is greater. The penetration range depends on the density of the material in which the β-particle travels and on the β-particle's kinetic energy. Fortunately, the typical penetration range of β-particles emitted by biologically relevant (e.g., ^{14}C, ^{33}P, ^{35}S, ^{45}Ca) and inert (e.g., ^{36}Cl) radio-isotopes in water lies between ~80 and ~800 μm (Table 1). Thus, the constructed microsensor permits measurements of tracers labeled with these elements in biological samples with a submillimeter spatial resolution.

Although the small sensor size is certainly required for achieving minimally invasive and high spatial resolution measurements, it seriously decreases the sensor sensitivity and thus requires high levels of radioactivity in the sample. For example, typical minimum radioactivity concentrations that can be measured by the sensor are 5–20 kBq cm^{-3} for ^{36}Cl, 100–300 kBq cm^{-3} for ^{45}Ca, and 100–600 kBq cm^{-3} for ^{14}C (see *LOD* in Table 2). Working with such high values in routine experiments may thus be permitted only if sample volumes are relatively small (e.g., a few cm^3 to several tens of cm^3) so that the total radioactivity does not exceed the limits imposed by safety regulations. Additionally, the decrease in sensitivity due to the small sensor size implies longer times to obtain one reading. As a "rule of thumb," one should accumulate ~100 photons in one measurement to achieve an acceptable signal-to-noise ratio. For example, depending on the sensor, a reliable reading can be obtained in 0.3–1.2 min for ^{36}Cl radioactivities around 500 kBq cm^{-3}, while 0.4–3 and 0.2–12 min are needed to detect ^{45}Ca and ^{14}C at radioactivities around 5 MBq cm^{-3}, respectively, as estimated from the typical sensitivities achieved by the constructed sensors shown in Table 2. The recommended accumulation times then increase proportionally as the volume-specific radioactivity decreases.

It must be stressed that radioactivity microsensor measurements must be carried out in total darkness, as the detectors attached to the sensor are capable of detecting single photons. Achieving this is not trivial, because even a tiny hole of ~100 μm in the light-shielding casing could result in an elevated signal. In this work we met this requirement by enclosing the entire measuring setup in a box, which was carefully sealed and painted black from the inside. Mechanical stability with submillimeter precision is also required during the measurements (e.g., achieved by mounting the sensor on a robust metal stand), since it takes several minutes to hours to acquire reliable signal and hours to days to complete an experiment. In this regard it should be pointed out that the microsensor is useful only in connection with radio-isotopes whose half-life times are sufficiently long (at least a few days) so that their radioactivity remains constant during the experiment.

In conclusion, the radioactivity microsensor presented in this work provides a useful extension of the suite of microsensors available for biogeochemical studies requiring high spatial resolution measurements. Certain technical improvements may be required to broaden the sensor applicability. Enhancement of the sensor sensitivity and *SNR*, which would allow use of lower radiotracer activities, is certainly one of them. This can be achieved by using a more efficient scintillating material for the detector sphere, if such material becomes available. Also, the efficiency with which the photons generated in the detector sphere are coupled into the fiber can further be improved, e.g., by optimizing the size of the sphere and the concentration of the light scattering particles dispersed in it, or by depositing a thin metal layer around the detector to act as a mirror reflecting photons into the fiber. Nevertheless, in its present form, the radioactivity microsensor can be used to measure (i) diffusion coefficients of complex (e.g., organic) molecules in a wide range of materials; (ii) diffusion coefficients in sediments/mats, i.e., substrates other than water + agar; (iii) spatial mapping of binding and release of pollutants; (iv) uptake of substrates. Provided that the sensitivity of the sensor is improved, the sensor may become a useful tool also in the medical and pharmaceutical research, e.g., (i) for the measurement of the arterial input function without the need of blood sampling; (ii) for the detection of β-labeled receptors in animal brains; (iii) for the measurement of activity of ^{18}F-labeled tumors during tumor operations.

References

Bungay, H. R., W. J. Whalen, and W. M. Sanders. 1969. Microprobe Techniques for Determining Diffusivities and Respiration Rates in Microbial Slime Systems. Biotechnol. Bioeng.11:765–766.

Gieseke, A., and D. De Beer. 2004. Use of microelectrodes to measure in situ microbial activities in biofilms, sediments, and microbial mats. In G. G. Kowalchuk, F. J. de Bruijn, I. M. Head, A. D. Akkermans, and J. D. van Elsas [eds.], Molecular Microbial Ecology Manual. Springer.

Jonkers, H. M. and others. 2003. Structural and functional analysis of a microbial mat ecosystem from a unique permanent hypersaline inland lake: 'La Salada de Chiprana' (NE Spain). FEMS Microbiol. Ecol. 44:175–189.

Jørgensen, B. B., and Y. Cohen. 1977. Solar Lake (Sinai). 5. The sulfur cycle of the benthic cyanobacterial mats. Limnol. Oceanogr. 22: 657–666.

Kühl, M., and N. P. Revsbech. 1999. Biogeochemical microsensors for boundary layer studies, p. 180–210. In B. P. Boudreau and B. B. Jørgensen [eds.], The benthic boundary layer. Oxford University Press.

Lassen, C., H. Ploug, and B. B. Jørgensen. 1992. A Fiberoptic Scalar Irradiance Microsensor – Application for Spectral Light Measurements in Sediments. FEMS Microbiol. Ecol. 86:247–254.

Li, Y.-H., and S. Gregory. 1974. Diffusion of ions in sea water and deep-sea sediments. Geochim. Cosmochim. Acta. 38:703–714.

Ludwig, R., F. A. Al-Horani, D. De Beer, and H. M. Jonkers. 2005. Photosynthesis-controlled calcification in a hypersaline microbial mat. Limnol. Oceanogr. 50:1836–1843.

Ludwig, R., O. Pringault, R. De Wit, D. De Beer, and H. M. Jonkers. 2006. Limitation of oxygenic photosynthesis and oxygen consumption by phosphate and organic nitrogen in a hypersaline microbial mat: a microsensor study. FEMS Microbiol. Ecol. 57:9–17.

Revsbech, N. P. 1983. In situ measurement of oxygen profiles of sediments by use of oxygene microelectrodes, p. 265-273. In E. Gnaigner and H. Forstner [eds.], Polarographic oxygen sensors: Aquatic and physiological applications. Springer.

———. 1989. An Oxygen Microsensor with a Guard Cathode. Limnol. Oceanogr. 34:474–478.

US Public Health Service (1970). Radiological Health Handbook. p. 461 Publ. No. 2016. Bureau of Radiological Health, Rockville, MD.

Lederer, C. M., and V. S. Shirley. 1978. Table of Isotopes, 7th Edition, Wiley, New York.

Submitted 11 February 2007
Revised 18 July 2007
Accepted 21 July 2007